minerals

MDPI

Article

First-Principles Density Functional Theory Characterisation of the Adsorption Complexes of H_3AsO_3 on Cobalt Ferrite (Fe_2CoO_4) Surfaces

Eloise C. Lewis and Nelson Y. Dzade *

School of Chemistry, Cardiff University, Main Building, Park Place, Cardiff CF10 3AT, UK; eloise23@btinternet.com

* Correspondence: DzadeNY@cardiff.ac.uk

Abstract: The mobility of arsenic in aqueous systems can be controlled by its adsorption onto the surfaces of iron oxide minerals such as cobalt ferrite (Fe_2CoO_4). In this work, the adsorption energies, geometries, and vibrational properties of the most common form of As(III), arsenous acid (H_3AsO_3), onto the low-index (001), (110), and (111) surfaces of Fe_2CoO_4 have been investigated under dry and aqueous conditions using periodic density functional theory (DFT) calculations. The dry and hydroxylated surfaces of Fe_2CoO_4 steadily followed an order of increasing surface energy, and thus decreasing stability, of (001) < (111) < (110). Consequently, the favourability of H_3AsO_3 adsorption increased in the same order, favouring the least stable (110) surface. However, by analysis of the equilibrium crystal morphologies, this surface is unlikely to occur naturally. The surfaces were demonstrated to be further stabilised by the introduction of H_2O/OH species, which coordinate the surface cations, providing a closer match to the bulk coordination of the surface species. The adsorption complexes of H_3AsO_3 on the hydroxylated Fe_2CoO_4 surfaces with the inclusion of explicit solvation molecules are found to be generally more stable than on the dry surfaces, demonstrating the importance of hydrogen-bonded interactions. Inner-sphere complexes involving bonds between the surface cations and molecular O atoms were strongly favoured over outer-sphere complexes. On the dry surfaces, deprotonated bidentate binuclear configurations were most thermodynamically favoured, whereas monodentate mononuclear configurations were typically more prevalent on the hydroxylated surfaces. Vibrational frequencies were analysed to ascertain the stabilities of the different adsorption complexes and to assign the As-O and O-H stretching modes of the adsorbed arsenic species. Our results highlight the importance of cobalt as a potential adsorbent for arsenic contaminated water treatment.

Keywords: cobalt ferrite (Fe_2CoO_4); arsenous acid (H_3AsO_3); adsorption complexes; density functional theory (DFT)

Citation: Lewis, E.C.; Dzade, N.Y. First-Principles Density Functional Theory Characterisation of the Adsorption Complexes of H_3AsO_3 on Cobalt Ferrite (Fe_2CoO_4) Surfaces. *Minerals* **2021**, *11*, 195. https://doi.org/10.3390/min11020195

Academic Editor: Jordi Ibanez-Insa
Received: 30 December 2020
Accepted: 5 February 2021
Published: 12 February 2021

1. Introduction

Water is a fundamental resource for the sustainment of life, and so it is essential that access to clean water for drinking, sanitation, and other uses is feasible globally. Inorganic arsenic is the most significant contaminant in the world's drinking water. It is highly toxic, with a lethal range of inorganic arsenic estimated to be 1–3 mg As kg^{-1}, and is thus well known to be used for its toxic properties [1]. Arsenical compounds occur naturally in water due to volcanic activity, weathering of rocks, solubilisation, and transport of sediment. They are also becoming increasingly present in the environment as a result of human activities and the use of herbicides, pesticides, and waste products, accelerated by erosion of land and combustion of fossil fuels [2].

Adsorption is a widely used technique for the removal of arsenic and other species from water and other systems [3]. The adsorption of arsenic species onto iron oxide and iron oxyhydroxide mineral surfaces has been at the centre of many studies [4–7]. There remains, however, ambiguity in the possible reactions and adsorption mechanisms of such techniques. Molecular-level insight into the interactions of arsenic species with different iron oxide mineral surfaces is essential to understanding the adsorption mechanisms. Owing to the complex reactions occurring at the mineral surfaces, it is experimentally difficult to predict the nature of the adsorption complexes; whether monodentate or bidentate bonding is energetically favoured. However, using computer simulations based on density functional theory (DFT) calculations, it is now possible to unravel the adsorption complexes of pollutant species on mineral surfaces at the atomic level. For example, Dzade et al., employed DFT calculations to unravel the structure and properties of $As(OH)_3$ adsorption complexes on mackinawite (FeS) [8] and ferrihydrite (110) [9] mineral surfaces. Goffinet and Mason employed spin-polarised DFT calculations to study inner-sphere As(III) complexes on hydrated α-Fe_2O_3(0001) surface models [10]. Corum et al., characterised the adsorption complexes of arsenate onto alumina surfaces using DFT calculations [11].

However, there is limited research dedicated to characterising the adsorption mechanism of arsenic on magnetic spinel B_2CoO_4 compounds (B = Cr, Mn, or Fe). Magnetic spinel materials have attracted a surge of interest recently for a wide range of applications including magnetic data storage, catalysis, and as contrast agents in magnetic resonance imaging, because of their high stability, resistance towards acid and alkali attacks, and magnetic properties [12]. Cobalt ferrite (Fe_2CoO_4) is a ferrimagnetic oxide like magnetite (Fe_3O_4). It exhibits remarkably unique and interesting properties such as high saturation magnetisation, high coercivity and anisotropy, good mechanical hardness, chemical stability, and has the highest magnetostriction of all 3*d*-element-based spinel oxides, with an additional benefit of being cheap and easy to make [13]. The preparation method and conditions of this spinel ferrite strongly influence the acquired degree of inversion and thus its properties [14–18]. In an investigation of the adsorption of both arsenite (H_3AsO_3) and arsenate (H_3AsO_4) on Fe_2MnO_4, Fe_2CoO_4 and Fe_3O_4, Zhang et al. synthesised the material via co-precipitation, an effective synthetic approach that permits good control of shape and particle size distribution [18,19]. It was demonstrated that the maximum adsorption capacities of arsenite and arsenate on Fe_2CoO_4 were 100 and 74 mg g^{-1}, respectively, which are higher than those for Fe_3O_4 (50 and 44 mg g^{-1}, respectively). This trend is in agreement with other experimental findings, indicating that cobalt ferrite has a greater potential for application in water purification [20].

Although there exist experimental studies about the magnetic properties and pollutants adsorption on Fe_2CoO_4 and its variants [13,18–20], there are no atomistic first-principles studies dedicated to characterising the fundamental adsorption process and complexation of arsenite onto the Fe_2CoO_4 surface, which makes this study timely. In the present study, we have employed computational approaches based on DFT to characterise the surface structures, compositions, and stabilities of the inverse spinel Fe_2CoO_4 mineral. Subsequently, the structures and energetics of arsenous acid (H_3AsO_3) adsorption complexes have been predicted under anhydrous and hydrous conditions. Geometrical parameters and vibrational frequency assignment of the As-O and O-H stretching modes are reported and discussed. These results improve our understanding of the adsorption reactions and complexation of H_3AsO_3 on different cobalt ferrite surfaces at the molecular level.

2. Materials and Methods

All calculations were carried out using the VASP –Vienna Ab initio Simulation Package [21]. The projected augmented wave (PAW) method was used to describe the interactions between the valence electrons and the cores. The exchange-correlation potential was calculated using the Perdew–Burke–Ernzerhof (PBE) generalised gradient approximation

(GGA) functional with a Hubbard correction (PBE+U), which accounts for the Coulomb interaction of localised *d*-electrons [22]. In this study, U_{eff} values of 4 eV for Fe and 5 eV for Co were found to provide sufficiently accurate lattice parameters, electronic, and magnetic properties of Fe_2CoO_4. Long-range van der Waals (vdW) interactions were accounted for using the method of Grimme (DFT-D3) [23]. A plane-wave basis set with a kinetic energy cut-off of 600 eV was tested to be sufficient to converge the total energy of Fe_2CoO_4 to within 10^{-6} eV. Geometry optimisations were performed based on the conjugate-gradient algorithm until the residual Hellmann–Feynman forces on all relaxed atoms reached 10^{-3} eV Å^{-1}. The Brillouin zone of the bulk Fe_2CoO_4 was sampled using a 5 × 5 × 5 Monkhorst-Pack K-point mesh [24].

The bulk Fe_2CoO_4 containing 56 atoms ($Fe_{16}Co_8O_{32}$) was modelled in the inverse spinel cubic structure with space group $Fd\bar{3}m$. The crystallographic information file (CIF) of the normal spinel structure obtained from the Materials Project online database was used to create the inverse spinel structure, which was then subjected to geometry optimisation in order to determine its lattice constant and structural parameters [25]. From the fully relaxed bulk Fe_2CoO_4 material, the commonly observed (001), (110), and (111) surfaces were created using the METADISE code [26]. In each simulation, a vacuum of 15 Å was added in the *c*-axis to avoid interactions between periodic slabs. The surfaces were optimised using a k-point mesh of 3 × 3 × 1. From calculated surface energies, the equilibrium morphology of the dry and hydroxylated Fe_2CoO_4 nanoparticles was predicted based on Wulff's construction as implemented in the GDIS visualisation software [27]. Different coordination modes of H_3AsO_3 were studied including bidentate binuclear (BB) and monodentate mononuclear (MM) configurations in order to find the most stable coordination complexes. Large area surface slabs were used to characterise H_3AsO_3 adsorption: the (001), (110), and (111) surfaces have a surface area of 72.82, 102.98, and 126.12 Å^2, respectively. The introduction of a single H_3AsO_3 molecule onto these large area surfaces ensured that the lateral interactions between the H_3AsO_3 species in neighbouring image cells, which may influence their adsorption geometries, are minimised. The strength of the adsorption for each adsorbate molecule (M) was determined by calculating the adsorption energy, (Eads) as follows:

$$E_{ads} = E_{surf+M} - (E_{surf} + E_M) \quad (1)$$

where E_{surf+M}, E_{surf}, and E_M are the total energies of the whole system (dry or solvated adsorbate on the adsorbent slab), relaxed dry or solvated surface, and adsorbate molecule (M = H_3AsO_3), respectively. When optimising these systems, the adsorbate and the topmost four surface layers were allowed to relax unconstrainedly, while the remaining bottom layers were kept fixed to mimic the bulk structure. The stabilities of the different predicted arsenic adsorption complexes were ascertained by calculating their vibrational frequencies, for which stable structures are characterised by positive vibrational frequencies.

3. Results

3.1. Bulk Properties

The inverse spinel Fe_2CoO_4 structure is characterised by half of the octahedral (O_h) sites being occupied by Co^{2+} cations and the other half of the octahedral sites and all of the tetrahedral (T_d) sites being occupied by Fe^{3+} cations (Figure 1a). After full relaxation of the bulk Fe_2CoO_4 unit cell, the lattice constant is determined to be a = 8.435 Å, which is in good agreement with experimental (a = 8.533 Å) and previous GGA+U (8.41−8.46 Å) values [28,29]. The optimised Co-O, Fe_{Oh}-O, and Fe_{Td}-O bond lengths are calculated at 2.10 Å, 2.04 Å, and 1.90 Å, respectively, in close agreement with previous GGA+U predictions [30]. In order to further investigate the material's electronic properties, the partial density of states (PDOS) of Fe_2CoO_4 was calculated as shown in Figure 1b. It is evident from the PDOS that the spin-up and spin-down density of states are asymmetric, confirming the characteristic ferrimagnetic nature of Fe_2CoO_4. The semiconducting behaviour of Fe_2CoO_4 is also well

reproduced, predicting a bandgap of approximately 1.82 eV. The valence band is found to be dominated by the 2*p* states of O, whereas the conduction band is dominated by the 3*d* states of Fe. The features of the PDOS in the present study are quite comparable to those obtained by Das et al. [28] and Hou et al. [30] with GGA+U methods, although they observed smaller bandgaps estimated at 1.14 eV and 0.72 eV, respectively. The average magnetic moments of the tetrahedral and octahedral Fe^{3+} ions in the bulk structure are predicted to be 4.016 and 4.154 μB, respectively (Table S1). The octahedral Co^{2+} ions on other hand have a magnetic moment of 2.696 μB. Previous work by Das et al. [28] predicted the magnetic moments to be 3.98, 4.10, and 2.66 μB for $Fe^{3+}{}_{Td}$, $Fe^{3+}{}_{Oh}$, and Co^{2+}, respectively, and Hou et al. [30] predicted similar values of 3.97, 4.10, and 2.61 μB, respectively.

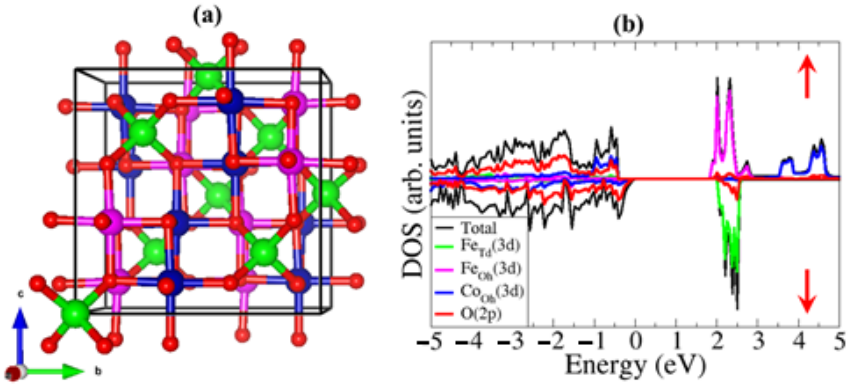

Figure 1. (**a**) Relaxed bulk structure and (**b**) partial density of states (PDOS) of inverse spinel Fe_2CoO_4 (atomic colour: Fe_{Td} = green (spin up), Fe_{Oh} = pink (spin down), Co = blue (spin down), O = red).

3.2. Surface Characterisation

The low-index (001), (110), and (111) surfaces were created from the fully relaxed bulk Fe_2CoO_4 structure. Shown in Figure 2 are the optimised surface structures for the most stable terminations of the dry (naked) (001), (110), and (111) surfaces. The topmost layer of the dry (001) surface (Figure 2a) is made up of two five-coordinate octahedral Co atoms (Co_{Oh}), two five-coordinate octahedral Fe (Fe_{Oh}) atoms, and one three-coordinate tetrahedral Fe (Fe_{Td}) atom, which sits slightly higher than the Fe_{Oh} atoms. The (110) surface (Figure 2b), however, has two three-coordinate Fe_{Oh} atoms on the topmost surface layer. The (111) surface (Figure 2c) contains a three-coordinate Co and four three-coordinate Fe atoms, one of which comes from an Fe_{Oh} in the bulk structure and is more raised than the others, which are Fe_{Td}. Another Fe_{Td} atom sits slightly lower than these, but still has all four of its bonds, and so is likely to be less reactive compared to the others nearby. All three surfaces contain a mixture of three- and four-coordinate oxygen atoms. Because of the decreased coordination number of the surface cations, we observed modification of their magnetic moments compared to the bulk to material (Table S1). In the case of the (001) surface, average values of 3.550 μB/Fe_{Td}, 4.092 μB/Fe_{Oh}, and 2.701 μB/Co were obtained. The (110) surface had two equivalent terminating Fe_{Oh} ions, both with a magnetic moment of 3.581 μB/Fe_{Oh}, whereas Fe_{Td} ions in the second layer have magnetic moment of 3.851 μB. The (111) surface gave average values of 3.932 μB/Fe_{Td}, 3.526 μB/Fe_{Oh}, and 2.599 μB/Co. The changes in these values compared with those in the bulk structure can be attributed to the decreased coordination numbers of the surface cations. This effect is less strong for the Co^{2+} surface cations and remains similar to bulk values. As the coordination number of the Fe_{Oh} decreased from 6 to 5 to 3, we see a coinciding change in magnetic moment from 4.154 μB in the bulk, to 4.092 μB for the five-coordinate Fe_{Oh} on the (001) surface, to approximately 3.550 μB on the other two surfaces. The magnetic moment of the Co^{2+} surface cations remains generally close those of the bulk magnetic moments.

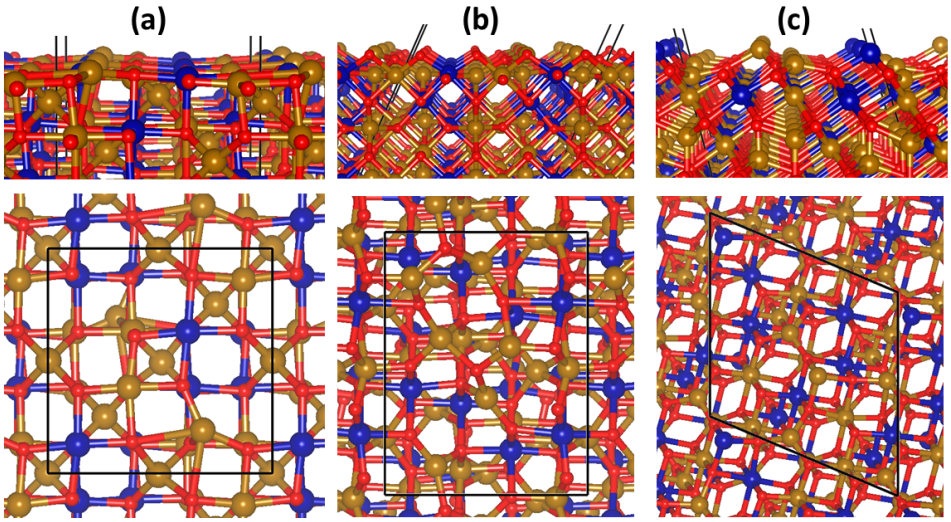

Figure 2. Optimised structures of the naked (**a**) (001), (**b**) (110), and (**c**) (111) surfaces of Fe_2CoO_4 side (up) and top (down) views (atomic colour: Fe = brown, Co = blue, O = red).

Considering that, in aqueous conditions, the surfaces may be hydrated (covered with water molecules) or hydroxylated (covered with OH species, resulting from water dissociation), we have first quantified the energetics of molecular and dissociative water adsorption on the three different surfaces. This is to ascertain whether the surfaces will preferentially be covered with molecular adsorbed water or OH species resulting from water dissociation. Generally, dissociative water adsorption is found to be energetically favoured over molecular water adsorption on all three surfaces (Supplementary Materials, Figure S1, Table S2), suggesting that the Fe_2CoO_4 surfaces will be hydroxylated under normal conditions. Having found that the water molecules will preferentially adsorb dissociatively on the Fe_2CoO_4 surfaces, we created a monolayer of OH-covered (001), (110), and (111) surfaces by introducing 7, 4, and 6 water molecules adsorbed dissociatively (Figure 3a–c). During energy minimisation, some of the OH/H species at the (001) surface recombined to form H_2O on the (001), two of which were physisorbed.

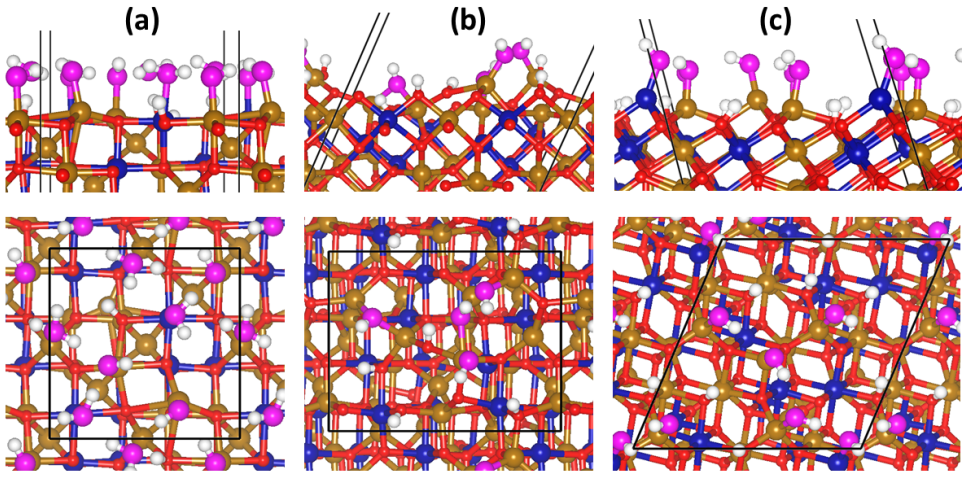

Figure 3. Optimised structures of H_2O/OH covered (**a**) (001), (**b**) (110), and (**c**) (111) surfaces of Fe_2CoO_4 in side (up) and top (down) views. H_2O molecules enlarged for clarity (Fe = brown, Co = blue, O_{surf} = red, O_{H2O} = purple, H = white).

Seeing that the hydration/hydroxylation may have a stabilising effect on the Fe_2CoO_4 surfaces, the relative stabilities of the Fe_2CoO_4 surfaces were determined by calculating

the surface energies of the dry surfaces (γ_r) and hydroxylated surfaces ($\gamma_{hydrox.}$) using Equations (2) and (3).

$$\gamma_r = \frac{E_{surf} - nE_{bulk}}{2A} \quad (2)$$

where E_{surf} is the energy of the slab, E_{bulk} is the energy of the bulk Fe_2CoO_4 material, n is the number of unit cells used in the slab, and A is the surface area of one side of the slab.

$$\gamma_{hydrox.} = \frac{E_{hydrox.} - xE_{H2O} - nE_{bulk}}{A} - \gamma_r \quad (3)$$

wherein $E_{hydrox.}$ is the energy of the relaxed hydroxylated surface, x is the number of H_2O molecules used to hydroxylate the surface, E_{H2O} is the energy of the isolated H_2O molecule, and γ_r is the relaxed surface energy of the corresponding surface, as determined by Equation (2). The relaxed surface energy of the dry surfaces is calculated at 1.454, 2.121, and 1.882 Jm^{-2} for the (001), (110), and (111) Fe_2CoO_4 surfaces, respectively. These results show that the order of increasing surface energy, and thus decreasing stability for the dry surfaces, follow the trend (001) < (111) < (110). When hydroxylated, the surface energy is predicted at −0.011, 0.993, and 0.596 Jm^{-2} for the (001), (110), and (111) Fe_2CoO_4 surfaces, respectively. In comparison with the dry surfaces, all surface energies were reduced considerably upon hydroxylation. Most notably, the (001) surface energy became negative, signifying that it is now significantly more stable than the other two hydroxylated surfaces. The order of stability remained as (001) < (111) < (110), as was predicted for the dry surfaces. Based on the calculated surface energies, the equilibrium morphology of the dry and hydroxylated Fe_2CoO_4 nanoparticles was predicted in order to determine which facets are present and/or dominant. For the dry nanoparticle (Figure 4a), it is observed that the crystal adopts a truncated cubic shape, with the most stable (001) surface having the largest surface area, followed by the second most stable surface, (111), truncating the corners of the cube. The absence of the (110) surface in the dry nanoparticle may be attributed to its relatively high surface energy [31]. The hydroxylated nanoparticle (Figure 4b), on the other hand, contains only the (001) lowest energy surface, forming a cubic crystal structure, consistent with its significant stabilisation upon hydroxylation relative to the other two surfaces. Although the surface energies of the (110) and (111) surfaces were also lowered considerably, these reductions were not significant enough to compete with the (001) surface for expression in the nanoparticle.

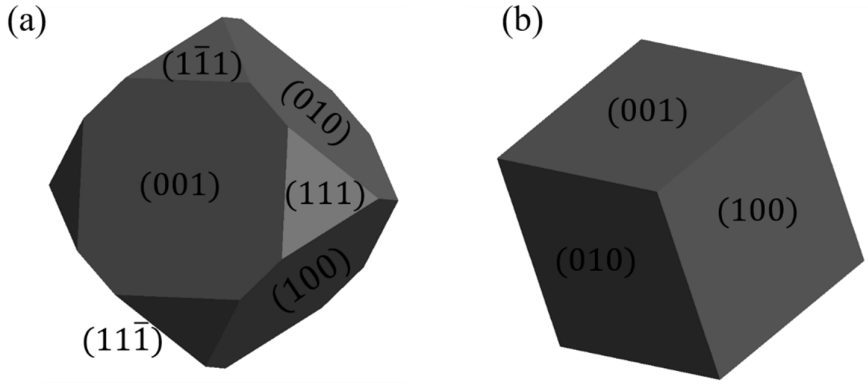

Figure 4. Wulff plots of the equilibrium morphologies of (**a**) the dry nanoparticle and (**b**) the hydroxylated nanoparticle of Fe_2CoO_4.

3.3. Adsorption Complexes of H_3AsO_3 on Dry Fe_2CoO_4 Surfaces

Although contamination of water by arsenic species is a more globally prevalent concern, we can benefit from investigating the adsorption of H_3AsO_3 in the absence of water, as arsenic-containing species such as H_3AsO_3 can be found in soils and sediments and other non-aqueous environments. Hence, the adsorption complexes and properties of H_3AsO_3 were investigated on the dry Fe_2CoO_4 surfaces. In order to find the most stable adsorption geometries, a variety of monodentate mononuclear (MM) and bidentate binuclear (BB) modes were explored. The resulting unique low-energy adsorption configurations are shown in Figure 5, with the calculated adsorption energies summarised in Table 1. On the (001) surface, the most thermodynamically favoured protonated monodentate mononuclear geometry, MM-O-Co, was formed by an O_{mol}-Co (2.082 Å), releasing an adsorption energy of −1.442 eV. In comparison with the isolated H_3AsO_3 molecule, the As-O bond of the O_{mol} atom bound to the surface had lengthened from 1.810 Å to 1.898 Å, while the other two bonds had shortened. The monodentate mononuclear MM-As-Co and MM-As-Fe geometries released adsorption energies of −0.841 and −0.611 eV, respectively. Two protonated bidentate adsorption complexes (Figure 5: BB-Fe-OO-Co and BB-Fe-OO-Fe), wherein the O_{mol} atoms interacts with either two Fe atoms or one Fe and one Co atom, were predicted and are further stabilised by the As atom being in close proximity with an O_{surf} below. The BB-Fe-OO-Co and BB-Fe-OO-Fe adsorption complexes released similar energies calculated at −1.411 eV and −1.279 eV, respectively. A most stable adsorption is predicted for the deprotonated H_3AsO_3 adsorption in a BB-Fe-OO-Fe_{dp} geometry (Figure 5), which released an adsorption energy of −2.224 eV. In this complex, one of the O_{mol} atoms bound to Fe is deprotonated to form a surface hydroxyl (OH) species. The deprotonated As-O bond length is reduced (1.712 Å) compared with the two protonated As-O (1.881 and 1.901 Å). An interesting observation at this surface was the formation of a stable trinuclear bidentate (TB) configuration (TB-Fe-O2O-Fe_{dp}) in which all three O_{mol} atoms were involved in binding to two adjacent Fe surface atoms, releasing an adsorption energy of −2.076 eV.

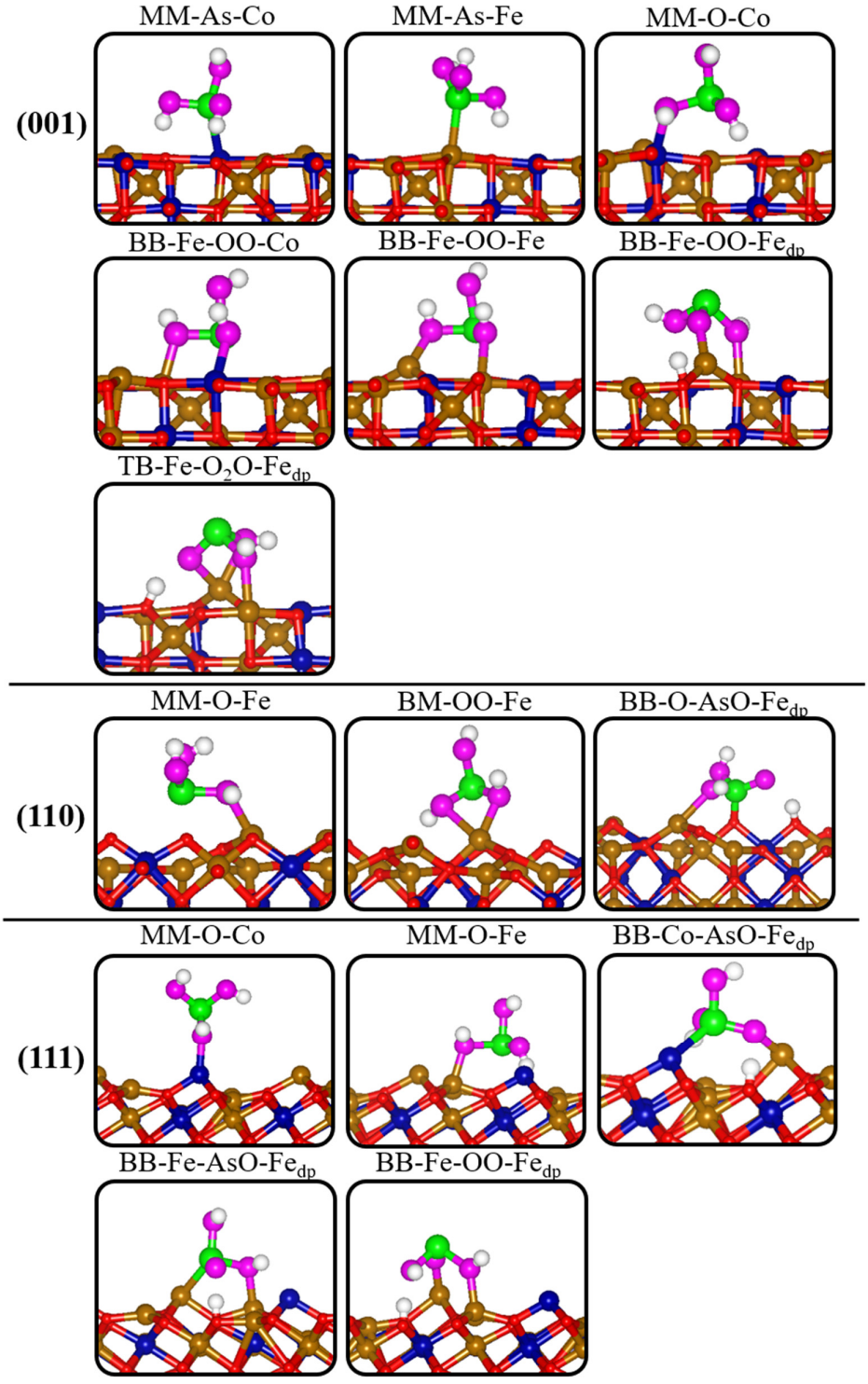

Figure 5. Optimised lowest-energy unique adsorption configurations of H_3AsO_3 on the dry Fe_2CoO_4 (001), (110), and (111) surfaces. H_3AsO_3 molecules enlarged for clarity (Fe = brown, Co = blue, O_{surf} = red, O_{mol} = purple, H = white); dp = deprotonated; MM = monodentate mononuclear; BB = bidentate binuclear.

Table 1. Calculated adsorption energies (eV) and bond lengths (Å) within the most stable unique adsorption geometries of H_3AsO_3 on dry Fe_2CoO_4 (001), (110), and (111) surfaces. O_{mol} = oxygen of adsorbing molecule, and O_{surf} = nearest surface oxygen (dp = deprotonated). MM = monodentate mononuclear; BB = bidentate binuclear.

Surface	Configuration	E_{ads}	$d_{As–O1}$	d_{As_O2}	d_{As-O3}	d_{Omol_M}	d_{As_M}	d_{As_Osurf}
	MM-As-Co	−0.841	1.797	1.786	1.802	3.370	2.647	2.973
	MM-As-Fe	−0.611	1.799	1.787	1.799	3.348	2.614	3.269
	MM-O-Co	−1.442	1.788	1.898	1.807	2.082	3.305	2.697
(001)	BB-Fe-OO-Co	−1.297	1.905	1.866	1.888	2.141,2.133	3.178	2.182
	BB-Fe-OO-Fe	−1.411	1.957	1.850	1.903	2.031,2.256	3.279	2.126
	BB-Fe-OO-Fe_{dp}	−2.224	1.881	1.712_{dp}	1.901	1.937_{dp},2.218	3.413	3.583
	TB-Fe-O_2O-Fe_{dp}	−2.076	1.927	1.886_{dp}	1.713	2.275,2.276,2.100_{dp}	2.963	3.740
(110)	MM-O-Fe	−1.505	1.911	1.807	1.831	2.141	3.497	2.550
	BM-OO-Fe	−1.832	1.836	1.870	1.809	2.158,2.434	2.992	2.653
	BB-O-AsO-Fe_{dp}	−3.942	1.653_{dp}	1.821	1.772	2.425	3.330	1.717
(111)	MM-O-Co	−0.943	1.812	1.880	1.785	2.034	3.551	4.565
	MM-O-Fe	−1.746	1.766	1.999	1.822	2.027	3.247	2.762
	BB-Co-AsO-Fe_{dp}	−2.130	1.756_{dp}	1.796	1.804	2.015_{dp}	2.731	3.554
	BB-Fe-AsO-Fe_{dp}	−2.250	1.680_{dp}	1.808	1.983	2.050	2.545	3.131
	BB-Fe-OO-Fe_{dp}	−3.262	1.861	1.702_{dp}	1.955	2.046,1.961_{dp}	3.394	3.791

The most stable intact H_3AsO_3 geometry on the (111) surface was bound by an O-Fe bond, releasing an adsorption energy of −1.746 eV. The As-O bond length of the O_{mol} atom bound to the surface increased to 1.999 Å. The equivalent structure with a monodentate O-Co bond instead had an adsorption energy of only −0.943 eV, indicating that this surface has more favourable interactions with the Fe surface atoms. This can be explained by the fact that the Fe ion involved here is tetrahedral, and so adsorption at this site would complete its coordination sphere, whereas, when adsorbing at Co sites, these are three-coordinate octahedral sites, so the coordination spheres remain incomplete upon adsorption with H_3AsO_3. This favourability can also be seen in comparing the adsorption energies of the two deprotonated bridging AsO geometries. The most thermodynamically stable deprotonated complex on the (111) surface is a BB-Fe-OO-Fe_{dp} geometry, in which one of the O atoms bound to Fe was deprotonated, releasing an adsorption energy of −3.262 eV. The other deprotonated BB-Co-AsO-Fe_{dp} and BB-Fe-AsO-Fe_{dp} released adsorption energies of −2.130 and −2.250 eV, respectively.

On the least stable (110) surface, the preferred H_3AsO_3 geometry turned out to be a bidentate mononuclear (BM) complex, BM-OO-Fe, in which two of the molecule's O atoms were bound to a single Fe_{Oh} surface atom with O-Fe bond lengths of 2.158 and 2.434 Å. The adsorption energy of the BM-OO-Fe complex is −1.832 eV, the most stable among all the protonated complexes on all three surfaces. These results show that the strength of adsorption is related to the stability of the surface, where the H_3AsO_3 binds most strongly to the least stable (110) surface. As expected, this surface also produced the most stable deprotonated adsorption complex (BB-O-AsO-Fe_{dp}), which released an adsorption energy of −3.942 eV. The deprotonated As-O bond length is predicted at 1.653 Å, which is shorter than the protonated As-O bond (1.821 and 1.772 Å). The most stable coordination modes are found to be the deprotonated complexes in which there is a proton transfer to form surface hydroxyl species. These results suggest that, on the dry Fe_2CoO_4 surfaces, H_3AsO_3 species will preferentially exist in deprotonated states.

3.4. Adsorption Complexes of H_3AsO_3 on Hydroxylated Fe_2CoO_4 Surfaces

The unique optimised geometries of H_3AsO_3 on the hydroxylated (001), (110), and (111) Fe_2CoO_4 surfaces are shown in Figure 6 and their structural properties are summarised in Table 2. Solvation effects were accounted for through the inclusion of four explicit water molecules near the H_3AsO_3 adsorbate on the (001), (110), and (111) surfaces. The adsorption of H_3AsO_3 onto the hydroxylated surfaces is found to be significantly stronger than on the dry surfaces. This is expected as the surface hydroxyl species and the solvating water molecules form hydrogen-bonding interactions with the H_3AsO_3 species, which

contribute to the stability of both the inner- and outer-sphere adsorption complexes on the hydroxylated surfaces. The most thermodynamically favourable of all adsorption geometries was the monodentate mononuclear MM-O-Co complex on the (001) surface, which was deprotonated and released an adsorption energy of −4.457 eV, which is almost twice the energy released by the MM-O-Co complex on the dry surface. The deprotonated As-O bond shortened to 1.737 Å and the remaining two As-O bonds lengthened compared with those in the non-aqueous system, owing to the additional hydrogen-bonded interactions introduced by the H_2O molecules. The strength of the hydrogen-bonded interactions in H_3AsO_3 adsorption complexes on the hydroxylated Fe_2CoO_4 surfaces is quantified by measuring all possible hydrogen-bonded interactions with nearest O_H_2O (solvated or adsorbed) and OH_{surf}, as shown in Table S3 (Supplementary Materials). In most cases, the interacting H---O_H_2O or H---OH_{surf} bond distances are less than 2 Å, indicating strong hydrogen-bonded interactions, which contributed to stabilising the H_3AsO_3 adsorption complexes. An outer-sphere complex (MM-O-Fe) on the (001) surface, wherein H_3AsO_3 is stabilised by weak van der Waals' and hydrogen-bonded interactions with the surrounding water molecules, released an adsorption energy of −2.127 eV. The lowest-energy adsorption complex on the (110) surface possesses an MM-O-Fe_{dp} geometry, wherein one H atom is transferred to the surface to form a surface hydroxyl species (i.e., deprotonation), releasing an adsorption energy of −3.941 eV compared with −3.128 eV for the non-deprotonated geometry on the (110) surface (MM-O-Fe). This is an almost twofold increase in stability upon solvation and, as a result, it also gives rise to a slightly shorter O_{mol}-M bond. In comparison with the non-aqueous equivalent, one O_{mol} again is deprotonated, shortening this bond, with the other two remaining relatively similar in length. The hydroxylated (111) surface yielded considerably more stable H_3AsO_3 adsorption complexes, with the most stable BB-Fe-OO-Fe configuration releasing an adsorption energy of −5.233 eV, compared with the MM-O-Co complex (−4.232 eV). The outer-sphere on the (111) surface released an adsorption energy of −1.934 eV. Compared with the dry surfaces, the adsorption of H_3AsO_3 on the on the hydroxylated surfaces with the inclusion of solvation effects is found to increase the stability of the H_3AsO_3 adsorption complexes on the Fe_2CoO_4 surfaces. Similar results were reported for H_3AsO_3 and H_3AsO_3 adsorption complexes on ferrihydrite (110) surface and for H_3AsO_3 adsorption complexes on hydrated mackinawite (FeS) surfaces.

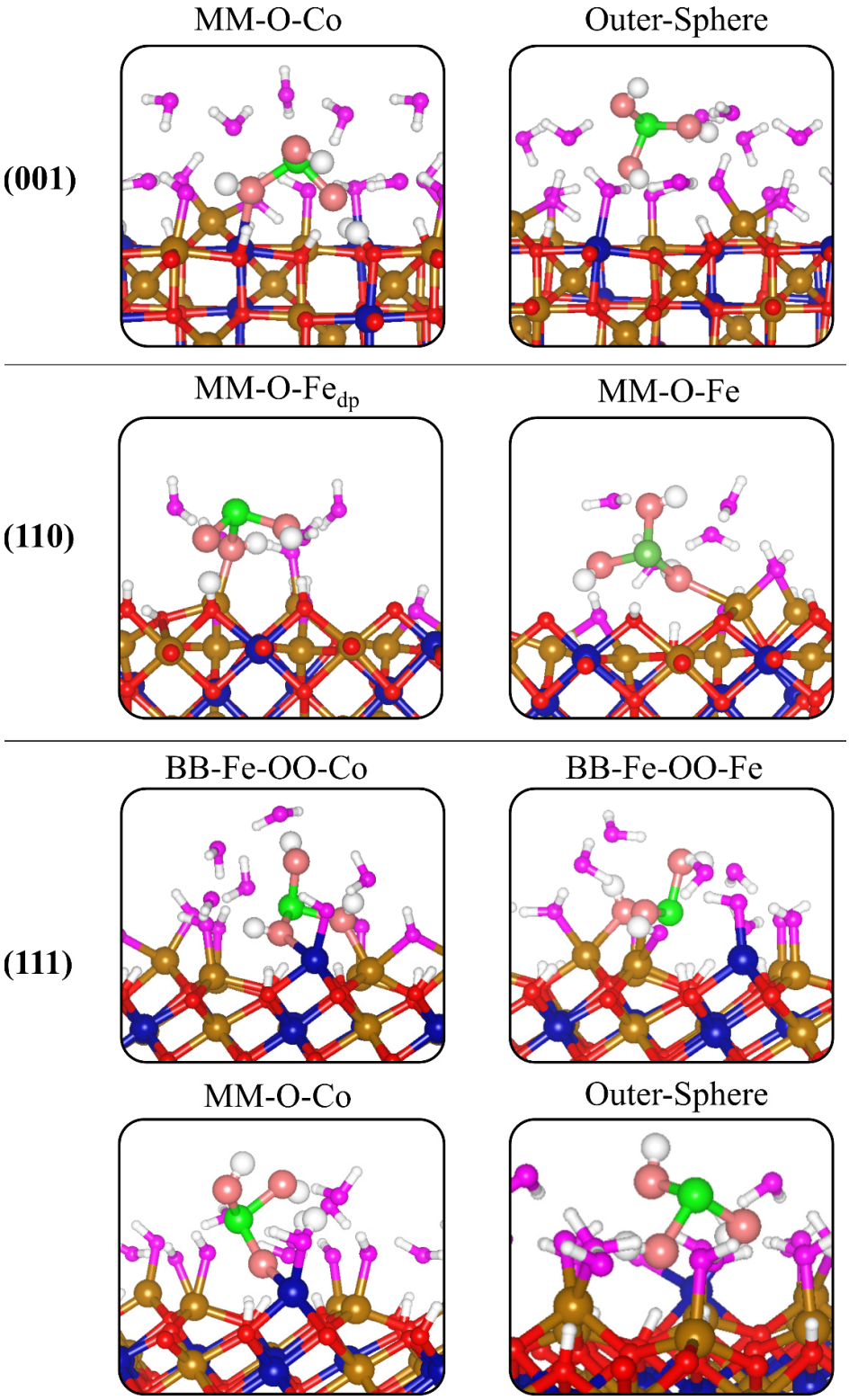

Figure 6. Optimised lowest-energy solvated unique configurations of H_3AsO_3 on hydroxylated Fe_2CoO_4 (001), (110), and (111) surfaces. H_3AsO_3 molecules enlarged for clarity (Fe = brown, Co = blue, O_{surf} = red, O_{H2O} = magenta O_{mol} = light pink, H = white).

Table 2. Adsorption energies (eV) and interatomic distances (Å) of each uniquely identified optimised geometry of H_3AsO_3 on hydroxylated Fe_2CoO_4 (001), (110), and (111) surfaces (dp = deprotonated, M = nearest surface Fe or Co cation).

Surface	Configuration	E_{ads}	d_{As-O1}	d_{As-O2}	d_{As-O3}	d_{Omol-M}	d_{As-M}	$d_{As-Osurf}$
001	MM-O-Co	−4.457	1.737_{dp}	1.877	1.938	2.160	3.711	3.450
	Outer-Sphere	−2.127	1.870	1.833	1769			
110	MM-O-Fe_{dp}	−3.941	1.821	2.006	1.716_{dp}	2.035	3.678	3.440
	MM-O-Fe	−3.128	1.825	1.892	1.842	2.289	3.804	2.580
111	BB-Fe-OO-Co	−3.440	1.785	1.881	1.824	2.099, 2.323	3.655	3.468
	BB-Fe-OO-Fe	−5.233	1.803	1.740_{dp}	1.925	2.141, 2.041_{dp}	3.269	3.127
	MM-O-Co	−4.232	1.861	1.749_{dp}	1.864	2.017	3.603	3.858
	Outer-Sphere	−1.934	1.785	1.790	1.879			

3.5. Vibrational Properties

In order to gain further insight into the stabilities of each uniquely identified adsorption complex on the dry and hydroxylated Fe_2CoO_4 surfaces, the vibrational frequencies of the adsorbed H_3AsO_3 species were calculated and the As-O and O-H stretching modes were assigned. These were also compared to the vibrational frequencies of the gas-phase H_3AsO_3 molecule. All predicted adsorption structures are deemed stable considering that almost all normal modes were positive, except for a few cases in which low imaginary modes were observed, corresponding to translational modes, and not to the As-O or O-H stretching modes. A clear and predictable trend is observed on the dry and hydroxylated surfaces, in which the bonds of the shortest length, and thus greatest strength, give rise to the highest vibrational frequencies. This is amplified for the deprotonated As-O bonds. The bond lengths for deprotonated As-O bonds are shortest, thus the atoms are more tightly bound and stable, resulting in a more rigid vibration of higher frequency. Tables 3 and 4 display the stretching As-O or O-H vibrational modes obtained for the dry and hydroxylated surfaces, respectively. The bond distances and corresponding stretching frequencies of all O-H bonds in H_3AsO_3 for all uniquely identified adsorption complexes on dry and hydroxylated Fe2CoO4 (001), (110), and (111) surfaces are provided in Tables S4 and S5 in the Supporting Information.

Table 3. Vibrational stretching frequencies of H_3AsO_3 in isolation (with experimental values from the literature) and of all uniquely identified adsorption complexes on dry Fe_2CoO_4 (001), (110), and (111) surfaces (dp = deprotonated).

		ν(As-O)/cm^{-1}			ν(O-H)/cm^{-1}		
Surface	**Configuration**	**As-O1**	**As-O2**	**As-O3**	**O1-H**	**O2-H**	**O3-H**
None	Isolated	606 (655) [32]	633 (655) [32]	662 (710) [32]	3831	3826	3692
	MM-As-Co	679	686	659	3401	3745	3574
	MM-As-Fe	664	693	649	3470	3797	3802
	MM-O-Co	702	522	647	3137	3483	3840
001	BB-Fe-OO-Co	520	590	544	3765	3746	3740
	BB-Fe-OO-Fe	454	642	530	3762	3775	3693
	BB-Fe-OO-Fe_{dp}	544	843_{dp}	501	3796	3289_{dp}	3807
	TB-Fe-O_2O-Fe_{dp}	498	554	822_{dp}	3797	3837	3295_{dp}
110	MM-O-Fe	514	657	599	3663	3826	3794
	BM-OO-Fe	612	556	623	3762	3707	2757
	BB-O-AsO-Fe_{dp}	938_{dp}	605	691	3503_{dp}	3732	3796
111	MM-O-Co	644	555	685	3815	3789	3679
	MM-O-Fe	735	435	631	2638	3757	3735
	BB-Co-AsO-Fe_{dp}	720_{dp}	665	650	3491_{dp}	3739	3480
	BB-Fe-AsO-Fe_{dp}	883_{dp}	649	406	2968_{dp}	3761	3666
	BB-Fe-OO-Fe_{dp}	560	452	851_{dp}	3789	3725	3436_{dp}

Table 4. Vibrational stretching frequencies of H_3AsO_3 in isolation (with experimental values from the literature) and of all uniquely identified adsorption complexes on hydroxylated Fe_2CoO_4 (001), (110), and (111) surfaces (dp = deprotonated).

		ν(As-O)/cm^{-1}			ν(O-H)/cm^{-1}		
Surface	**Configuration**	**As-O1**	**As-O2**	**As-O3**	**O1-H**	**O2-H**	**O3-H**
001	MM-O-Co	760_{dp}	560	472	3041_{dp}	2768	3422
	Outer-Sphere	553	622	725	3728	3174	2566
110	MM-O-Fe_{dp}	639	440	789_{dp}	2462	3029	2624_{dp}
	MM-O-Fe	639	529	603	3340	3038	3590
111	BB-Fe-OO-Co	695	559	654	2980	2568	2453
	BB-Fe-OO-Fe	656	758_{dp}	483	2482	3206_{dp}	3328
	MM-O-Co	598	773_{dp}	577	2801	3050_{dp}	3767
	Outer-Sphere	725	671	538	2535	2916	3844

The three most stable configurations on the (001) surface, as determined by their adsorption energies, are those that do not give rise to any imaginary vibrational frequencies in this analysis, confirming their thermodynamic stability. The most stable protonated adsorbing geometry is the MM-O-Co configuration, and it is the only protonated geometry on this surface with no imaginary frequencies. Its weakest As-O bond with a frequency of 522 cm^{-1} is given by the O molecule bound directly to the Co surface atom. It is seen that increased coordination onto the surface causes a weakening of the bonds directly involved in the coordination, and hence reduces the vibrational frequencies. This is seen for example in the values obtained for the tridentate binuclear (TB) geometry TB-Fe-O_2O-Fe_{dp}, in which all three O_{mol} atoms are involved in binding to the surface. The weakest As-O bond of length 1.927 Å is, as a result, the bond with the lowest vibrational frequency of 498 cm^{-1}. This configuration displays a significant weakening of two As-O bonds, whereas the third is strengthened considerably due to deprotonation. The O-H bond vibrations for deprotonated bonds expectedly decrease as the H atoms are now further from their O_{mol} atoms and instead bound to O_{surf} atoms, and the greater the strengthening of the As-O bond, the greater the weakening of the O-H bond. Similar observations were made for the dry (110) and (111) surfaces. The (110) BB-O-AsO-Fe_{dp} configuration gives rise to the strongest deprotonated As-O bond with a very high frequency of 938 cm^{-1}. Albeit having only three small imaginary frequencies, the MM-O-Co configuration on the (111) surface contained the most imaginary frequencies of all configurations. Its adsorption energy of −0.943 eV is significantly lower than the other configurations at this surface, and so, although it is still sufficiently stable, it is least likely to occur in a real system. Furthermore, this configuration is the one that most resembles the frequencies of those in the isolated H_3AsO_3 molecule.

No imaginary frequencies were found for any of the solvated H_3AsO_3 adsorption complexes on the hydroxylated surfaces, suggesting that they are all stable, more so than those on the dry surfaces. As seen in Table 4, the As-O bond stretching frequencies are generally greater for the outer sphere, physisorbed, H_3AsO_3 complexes than the inner-sphere, chemisorbed complexes, except when those O_{mol} atoms are deprotonated, again highlighting the weakening of these bonds upon adsorption onto the surfaces. As shown in Table S5, we observed elongation (>1 Å) of the O-H bonds (reduction in stretching frequencies), most especially for those for those forming hydrogen bonds with the surrounding O atoms of the surface hydroxyl groups and water molecules. The elongated O-H bonds and the deprotonated O-H ones are found to have stretching frequencies below 2600 cm^{-1}, whereas the shorter O-H bonds (<1 Å) are typically characterised by higher frequencies >3000 cm^{-1}. The change in the O-H bonds follows the same reasoning as above, in which longer bonds give rise to lower frequencies.

4. Conclusions

Using periodic DFT+U calculations, we have performed an atomistic-level investigation of the adsorption of H_3AsO_3 onto the low-index Fe_2CoO_4 (001), (110), and (111) sur-

faces under dry and aqueous conditions, including analysis of the coordination geometries, electronic, and vibrational properties. The strength of H_3AsO_3 adsorption is demonstrated to be related to the stability of different surfaces; it increases in the order (001) < (111) < (110). Along with the Wulff plots of the crystal morphologies, the surface energies of both sets of surfaces suggest that the reactive (110) surface is unlikely to exist unless engineered to be present in the structure. Hydroxylated surfaces were highly favoured over hydrated ones, indicating that these systems would operate optimally under intermediate-to-high pH conditions. The adsorbing H_2O/OH species also bring the coordination of the surface atoms closer to that in the bulk material, stabilising the surfaces. H_3AsO_3 also tended towards deprotonation, which can be attributed to the fact that less energy is required to break a weak O-H bond in H_3AsO_3 than what is released upon forming an O_{surf}-H bond. Monodentate mononuclear geometries were more prevalent than bidentate geometries and were largely the more thermodynamically favoured configurations in the solvated systems. In the absence of water, deprotonated bidentate binuclear geometries were generally more favourable. Solvation of the systems is found to enhance adsorption due to the introduction of hydrogen-bonding interactions between the H_3AsO_3 molecule and surrounding water species on the surface and in solution. The vibrational frequencies associated with each coordination mode and the crystal morphologies further support these findings and provide additional useful insight for future research into this system for arsenic adsorption. The adsorption characteristics of H_3AsO_3 on Fe_2CoO_4 surfaces in the present study are similar to, but are overall stronger than, those observed on the iron-containing materials ferrihydrite and mackinawite, highlighting its capacity to be a potential adsorbent over other alternatives [9,33]. It is thus expected that these results should be comparable to those of other iron oxides and ferrites that may be investigated in the future. The work presented in this report provides a good foundation for further computational and experimental research into this H_3AsO_3-Fe_2CoO_4 system and provides a molecular-level understanding of the adsorption mechanisms. Future investigations may expand the work presented here to include the effects of coverage (larger surface areas and multiple H_3AsO_3 species), surface defects (oxygen vacancies), and the use of classical molecular dynamics (MD) simulations, which will provide a complete description of the dynamic processes occurring at the H_3AsO_3-water-Fe_2CoO_4 interfaces.

Supplementary Materials: The following are available online at www.mdpi.com/2075-163X/11/2/195/s1, Figure S1: Low-energy adsorption geometries for molecular and dissociative H_2O on the Fe_2CoO_4 (001), (110), and (111) surfaces (Fe = brown, Co = blue, O_{surf} = red, O_{mol} = purple, H = white), Table S1: Magnetic moments of Fe_{Td}, Fe_{Oh}, and Co atoms in the bulk and surfaces of Fe_2CoO_4, Table S2: Adsorption energies and O_{mol}-metal bond lengths of molecular and dissociated H_2O geometries on the Fe_2CoO_4 surfaces, Table S3: Strength of hydrogen bonded interactions with nearest H-O_H_2O or H-OH_surf in all uniquely identified adsorption complexes of H_3AsO_3 on hydroxylated Fe_2CoO_4 surfaces, Table S4: Bond distances and corresponding stretching frequencies of O-H bonds in H_3AsO_3 adsorption complexes on dry Fe_2CoO_4 surfaces, Table S5: Bond distances and corresponding stretching frequencies of O-H bonds in H_3AsO_3 adsorption complexes on hydroxylated Fe_2CoO_4 surfaces.

Author Contributions: Data curation, E.C.L.; Formal analysis, E.C.L.; Funding acquisition, N.Y.D.; Supervision, N.Y.D.; Writing—original draft, E.C.L.; Writing—review & editing, N.Y.D. All authors have read and agreed to the published version of the manuscript.

Funding: Please add: This work is funded by the U.K. Engineering and Physical Sciences Research Council (EPSRC) for funding (Grant No. EP/S001395/1).

Data Availability Statement: Information on the data that underpins the results presented here, including how to access them, can be found in the Cardiff University data catalogue at http://doi.org/10.17035/d.2021.0128750010.

Acknowledgments: The simulations were performed using the computational facilities of the Advanced Research Computing @ Cardiff (ARCCA) Division, Cardiff University. This work also made

use of the facilities of ARCHER (http://www.archer.ac.uk), the U.K.'s national supercomputing service via our membership of the U.K.'s HEC Materials Chemistry Consortium, which is funded by EPSRC (EP/L000202).

Conflicts of Interest: The authors declare no conflict of interest.

References

1. Hughes, M.F. Arsenic toxicity and potential mechanisms of action. *Toxicol. Lett.* **2002**, *133*, 1–16.
2. Ferguson, J.F.; Gavis, J. A review of the arsenic cycle in natural waters. *Water Res.* **1972**, *6*, 1259–1274.
3. Nicomel, N.R.; Leus, K.; Folens, K.; Van Der Voort, P.; Du Laing, G. Technologies for arsenic removal from water: Current status and future perspectives. *Int. J. Environ. Res. Public Health* **2016**, *13*, 62.
4. Yean, S.; Cong, L.; Yavuz, C.T.; Mayo, J.T.; Yu, W.W.; Kan, A.T.; Colvin, V.L.; Tomson, M.B. Effect of magnetite particle size on adsorption and desorption of arsenite and arsenate. *J. Mater. Res.* **2005**, *20*, 3255–3264.
5. Giménez, J.; Martínez, M.; de Pablo, J.; Rovira, M.; Duro, L. Arsenic sorption onto natural hematite, magnetite, and goethite. *J. Hazard. Mater.* **2007**, *141*, 575–580.
6. Mayo, J.T.; Yavuz, C.; Yean, S.; Cong, L.; Shipley, H.; Yu, W.; Falkner, J.; Kan, A.; Tomson, M.; Colvin, V.L. The effect of nanocrystalline magnetite size on arsenic removal. *Sci. Technol. Adv. Mater.* **2007**, *8*, 71–75.
7. Jain, A.; Raven, K.P.; Loeppert, R.H. Arsenite and arsenate adsorption on ferrihydrite: Surface charge reduction and net OH^- release stoichiometry. *Environ. Sci. Technol.* **1999**, *33*, 1179–1184.
8. Dzade, N.Y.; Roldan, A.; de Leeuw, N.H. The surface chemistry of NOx on mackinawite (FeS) surfaces: A DFT-D2 study. *Phys. Chem. Chem. Phys.* **2014**, *16*, 15444–15456.
9. Dzade, N.Y.; De Leeuw, N.H. Density functional theory characterization of the structures of H_3AsO_3 and H_3AsO_4 adsorption complexes on ferrihydrite. *Environ. Sci. Process. Impacts* **2018**, *20*, 977–987.
10. Goffinet, C.J.; Mason, S.E. Comparative DFT study of inner-sphere As(III) complexes on hydrated α-Fe_2O_3(0001) surface models. *J. Environ. Monit.* **2012**, *14*, 1860–1871.
11. Corum, K.W.; Tamijani, A.A.; Mason, S.E. Density Functional Theory Study of Arsenate Adsorption onto Alumina Surfaces. *Minerals* **2018**, *8*, 91.
12. Jauhar, S.; Kaur, J.; Goyal, A.; Singhal, S. Tuning the properties of cobalt ferrite: A road towards diverse applications. *RSC Adv.* **2016**, *6*, 97694–97719.
13. Turtelli, R.S.; Kriegisch, M.; Atif, M.; Grössinger, R. Co-ferrite-A material with interesting magnetic properties. In Proceedings of the IOP Conference Series: Materials Science and Engineering, Islamabad, Pakistan, 23–27 September 2013; Volume 60.
14. Olsson, R.T.; Salazar-Alvarez, G.; Hedenqvist, M.S.; Gedde, U.W.; Lindberg, F.; Savage, S.J. Controlled synthesis of near-stoichiometric cobalt ferrite nanoparticles. *Chem. Mater.* **2005**, *17*, 5109–5118.
15. Maaz, K.; Mumtaz, A.; Hasanain, S.K.; Ceylan, A. Synthesis and Magnetic Properties of Cobalt Ferrite ($CoFe_2O_4$) Nanoparticles Prepared by Wet Chemical Route. *J. Magn. Magn. Mater.* **2007**, *308*, 289–295.
16. Sivakumar, M.; Kanagesan, S.; Babu, R.S.; Jesurani, S.; Velmurugan, R.; Thirupathi, C.; Kalaivani, T. Synthesis of $CoFe_2O_4$ powder via PVA assisted sol-gel process. *J. Mater. Sci. Mater. Electron.* **2012**, *23*, 1045–1049.
17. Girgis, E.; Tharwat, C.; Adel, D. Ferrites Nanoflowers for Dye Removal Applications. *J. Adv. Nanomater.* **2016**, *1*, 49–56.
18. Hosni, N.; Zehani, K.; Bartoli, T.; Bessais, L.; Maghraoui-Meherzi, H. Semi-hard magnetic properties of nanoparticles of cobalt ferrite synthesized by the co-precipitation process. *J. Alloys Compd.* **2017**, *694*, 1295–1301.
19. Zhang, S.; Niu, H.; Cai, Y.; Zhao, X.; Shi, Y. Arsenite and arsenate adsorption on coprecipitated bimetal oxide magnetic nanomaterials: MnFe2O4 and $CoFe_2O_4$. *Chem. Eng. J.* **2010**, *158*, 599–607.
20. Martinez-Vargas, S.; Martínez, A.I.; Hernández-Beteta, E.E.; Mijangos-Ricardez, O.F.; Vázquez-Hipólito, V.; Patiño-Carachure, C.; Hernandez-Flores, H.; López-Luna, J. Arsenic adsorption on cobalt and manganese ferrite nanoparticles. *J. Mater. Sci.* **2017**, *52*, 6205–6215.
21. Kresse, G.; Furthmüller, J. Efficiency of ab-initio total energy calculations for metals and semiconductors using a plane-wave basis set. *Comput. Mater. Sci.* **1996**, *6*, 15–50.
22. Perdew, J.P.; Burke, K.; Ernzerhof, M. Generalized Gradient Approximation Made Simple. *Phys. Rev. Lett.* **1996**, *77*, 3865–3868.
23. Grimme, S.; Antony, J.; Ehrlich, S.; Krieg, H. A consistent and accurate ab initio parametrization of density functional dispersion correction (DFT-D) for the 94 elements H-Pu. *J. Chem. Phys.* **2010**, *132*, 154104.
24. Monkhorst, H.J.; Pack, J.D. special points for Brillouin-zone integrations. *Phys. Rev. B* **1976**, *13*, 5188–5192.
25. Materials Project. Available online: https://materialsproject.org/materials/mp-753222/ (accessed on 16 February 2020).
26. Watson, G.W.; Kelsey, E.T.; De Leeuw, N.H.; Harris, D.J.; Parker, S.C. Atomistic simulation of dislocations, surfaces and interfaces in MgO. *J. Chem. Soc. Faraday Trans.* **1996**, *92*, 433–438.
27. Fleming, S.; Rohl, A. GDIS: A visualization program for molecular and periodic systems. *Zeitschrift fur Krist.* **2005**, *220*, 580–584.
28. Das, D.; Biswas, R.; Ghosh, S. Systematic analysis of structural and magnetic properties of spinel CoB_2O_4 (B = Cr, Mn and Fe) compounds from their electronic structures. *J. Phys. Condens. Matter* **2016**, *28*, 1–9.
29. Fritsch, D.; Ederer, C. Epitaxial strain effects in the spinel ferrites CoFe2 O4 and $NiFe_2O_4$ from first principles. *Phys. Rev. B Condens. Matter Mater. Phys.* **2010**, *82*, 1–11.

30. Hou, Y.H.; Zhao, Y.J.; Liu, Z.W.; Yu, H.Y.; Zhong, X.C.; Qiu, W.Q.; Zeng, D.C.; Wen, L.S. Structural, electronic and magnetic properties of partially inverse spinel $CoFe_2O_4$: A first-principles study. *J. Phys. D. Appl. Phys.* **2010**, *43*, 1–7.
31. Santos-Carballal, D.; Roldan, A.; Grau-Crespo, R.; De Leeuw, N.H. A DFT study of the structures, stabilities and redox behaviour of the major surfaces of magnetite Fe_3O_4. *Phys. Chem. Chem. Phys.* **2014**, *16*, 21082–21097.
32. Tossell, J.A. Theoretical studies on arsenic oxide and hydroxide species in minerals and in aqueous solution. *Geochim. Cosmochim. Acta* **1997**, *61*, 1613–1623.
33. Dzade, N.Y.; Roldan, A.; De Leeuw, N.H. Structures and Properties of $As(OH)_3$ Adsorption Complexes on Hydrated Mackinawite (FeS) Surfaces: A DFT-D2 Study. *Environ. Sci. Technol.* **2017**, *51*, 3461–3470.